Tensile and shear loading of four fcc high-entropy alloys: A first-principles study

Xiaoqing Li,[1,2,3,*] Stephan Schönecker,[1] Wei Li,[4] Lajos K. Varga,[3] Douglas L. Irving,[2] and Levente Vitos[1,3,4]

[1]*Applied Materials Physics, Department of Materials Science and Engineering, KTH-Royal Institute of Technology, Stockholm SE-10044, Sweden*

[2]*Department of Materials Science and Engineering, North Carolina State University, Raleigh, North Carolina 27695, USA*

[3]*Research Institute for Solid State Physics and Optics, Wigner Research Center for Physics, Budapest H-1525, P.O. Box 49, Hungary*

[4]*Department of Physics and Astronomy, Division of Materials Theory, Uppsala University, Box 516, SE-75120, Uppsala, Sweden*

(Received 12 December 2017; published 7 March 2018)

Ab initio density-functional calculations are used to investigate the response of four face-centered-cubic (fcc) high-entropy alloys (HEAs) to tensile and shear loading. The ideal tensile and shear strengths (ITS and ISS) of the HEAs are studied by employing first-principles alloy theory formulated within the exact muffin-tin orbital method in combination with the coherent-potential approximation. We benchmark the computational accuracy against literature data by studying the ITS under uniaxial [110] tensile loading and the ISS for the $[11\bar{2}](111)$ shear deformation of pure fcc Ni and Al. For the HEAs, we uncover the alloying effect on the ITS and ISS. Under shear loading, relaxation reduces the ISS by ∼50% for all considered HEAs. We demonstrate that the dimensionless tensile and shear strengths are significantly overestimated by adopting two widely used empirical models in comparison with our *ab initio* calculations. In addition, our predicted relationship between the dimensionless shear strength and shear instability are in line with the modified Frenkel model. Using the computed ISS, we derive the half-width of the dislocation core for the present HEAs. Employing the ratio of ITS to ISS, we discuss the intrinsic ductility of HEAs and compare it with a common empirical criterion. We observe a strong linear correlation between the shear instability and the ratio of ITS to ISS, whereas a weak positive correlation is found in the case of the empirical criterion.

DOI: 10.1103/PhysRevB.97.094102

I. INTRODUCTION

The development of high strength structural materials with good ductility has long been a main topic of experimental as well as theoretical interest. In real materials, strength and ductility are usually influenced by complex microstructural properties associated with defects, e.g., dislocations, cracks, and grain boundaries. However, if such defects were not present, the strength would be limited by the stress at which the lattice itself becomes unstable with respect to a homogeneous strain. This maximum stress is referred to as the ideal (or theoretical) strength, which has been recognized as a key parameter in understanding the mechanical behavior of solid materials [1–3]. The ideal strength has been involved in determining intrinsic ductility/brittleness [4,5], in modern theories of plasticity and fracture [3,6–8], prediction of the Peierls-Narbarro stress [9], estimating the length of twin bands [10], calibration of semiempirical interatomic potentials that are used for the study of extended defects [11–13], and identifying gum metals [14].

Theoretically, several approaches have been proposed to assess the ideal strength. For instance, the earliest estimations assumed simple analytic forms for the stress-strain relation, which made it possible to predict the ideal strength in terms of elastic constants [3,15]. Later, semiempirical pair potential and embedded atom models were adopted to predict them [16,17]. With the advent of density-functional theory (DFT) and efficient electronic structure methods, calculations of the ideal strength have become routine for a wide variety of bulk materials (pure metals, semiconductors, and compounds) and yield reliable values [2,5,18–24]. On the experimental side, recent material processing techniques allow to make nanocrystalline or microcrystalline metals containing a low defect density, such as whiskers, nanowires, and nanopillars. This offers the opportunity to observe ultrahigh strength and large elastic strains close to the theoretical limits [3,25–28]. For example, the maximum shear strength of single-crystalline Mo nanopillars determined from nanoindentation measurement is 15.8–16.7 GPa [26], which agrees very well with the theoretical value 17.6–18.8 GPa [29]. However, the ideal strength of alloys is still a young and mostly unexplored research area.

The recently developed high-entropy alloys (HEAs) containing several equimolar or near equimolar elements represent a new field in material design [30,31]. The solid solution phases of HEAs are often face-centered cubic (fcc), body-centered cubic (bcc), or hexagonal-close packed. It was found that some HEAs in fcc solid solution phase composed of the elements Cr, Mn, Fe, Co, and Ni, such as CrCoNi and CrMnFeCoNi, normally exhibit many appealing properties [31–34], e.g., high hardness, high yield strength, excellent resistance to irradiation damage, good wear resistance, and stable microstructure against heat treatment, which make them attractive for a wide range of applications. For these HEAs, despite the investigations of phase stability [35–37], mechanisms of defect dynamics [38], and the deformation

*xiaoqli@kth.se

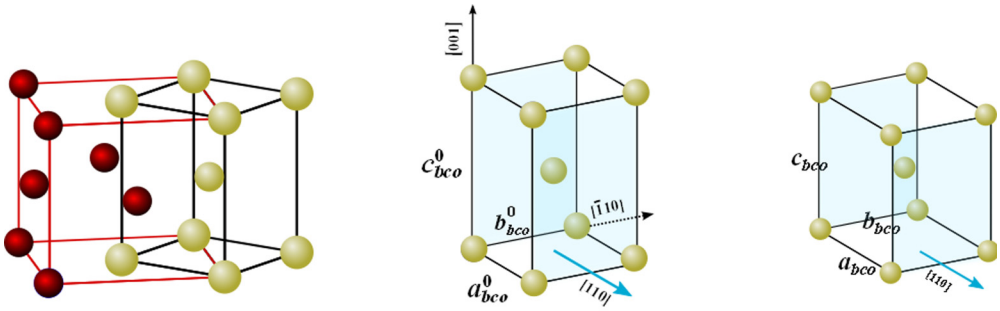

(a) (b) (c)

FIG. 1. Schematic for the bco structure used to model the uniaxial tension of an fcc crystal in the [110] direction: (a) the employed bco unit cell embedded in the fcc structure (coincides with the body-centered tetragonal representation of the fcc cell), (b) unstrained bco structure, (c) strained bco structure. The high-symmetry directions refer to the fcc structure.

mechanisms responsible for mechanical properties [33,39,40], the exploration of their intrinsic strength and ductility is still lacking. In this work, we make an attempt to fill this gap by studying the alloying effect on the ideal tensile strength (ITS) and ideal shear strength (ISS), and intrinsic ductility of four paramagnetic (PM) fcc HEAs, CrCoNi, CrFeCoNi, CrMnFeCoNi, and $Cr_{10}Mn_{40}Fe_{40}Co_{10}$, by means of DFT calculations. These four $3d$ transition metal HEAs were selected because they were successfully synthesized as single-phase solid solutions in the fcc structure, and their magnetic properties were characterized [31,34,41–44]. Using the obtained ISS, we lend further fundamental insight into the alloying effect on the half-width of the dislocation core that is involved in studying the plastic deformation behavior of materials.

Our work will facilitate a broader use of the ideal strength, for example, in previously established theories of intrinsic ductility. Furthermore, since the ideal strength sets the upper limit to the attainable strength, our results enable researchers to assess the gap remaining between the ideal strength and the best achievable strength of HEAs. Our investigations are expected to provide a guideline for further optimizing HEAs.

II. COMPUTATIONAL METHOD

A. Ideal tensile strength

In this study, we are concerned with the ITS of fcc HEAs loaded in the [110] direction. From previous studies for fcc elements [17,45,46], it is expected that the minimum ITS occurs in this direction. Figure 1 shows the employed body-centered orthorhombic (bco) computational cell in the unstrained state [Figs. 1(a) and 1(b)] and the strained state [Fig. 1(c)]. In the absence of strain, the three lattice parameters of the bco cell are $(a^0_{\rm bco}, b^0_{\rm bco}, c^0_{\rm bco}) = (\sqrt{2}/2,\ \sqrt{2}/2,\ 1)\ a_{\rm fcc}$, where $a_{\rm fcc}$ is the fcc equilibrium lattice parameter. It should be noted that the bco cell in the zero-strain state coincides with the body-centered tetragonal representation of the fcc cell. Under distortion, a uniaxial tensile strain ϵ was applied along the [110] direction (parallel to $\vec{a}$), and at each applied ϵ, the two unit-cell lattice vectors perpendicular to the [110] direction ($\vec{b}$ and $\vec{c}$) were relaxed [Fig. 1(c)]. From this quasistatic procedure, we obtained energy versus strain curves and derived stress versus strain data. The true stress $\sigma(\epsilon)$ versus engineering strain ϵ relation is given by

$$\sigma(\varepsilon) = \frac{1+\varepsilon}{\Omega(\varepsilon)}\frac{\partial E}{\partial \varepsilon}, \tag{1}$$

here $\Omega(\varepsilon)$ is the volume per atom at a given tensile strain ϵ, and E is the strain energy. The engineering strain ϵ of the simulation cell in the [110] direction is defined as

$$\epsilon = \frac{a_{\rm bco} - a^0_{\rm bco}}{a^0_{\rm bco}}, \tag{2}$$

where $a_{\rm bco}$ and $a^0_{\rm bco}$ denote the lengths of the cell parallel to the applied force in the strained and initial states (without distortion), respectively. The first maximum on the stress-strain curve (1) defines the ITS $\sigma_{\rm m}$ with corresponding maximum strain $\epsilon_{\rm m}$.

The relevant tensile modulus E relating stress and strain in the linear regime along the [110] direction is defined as [47]

$$E_{[110]} = \frac{\nu_{[110]}}{C_{12}}\left[C_{11}(C_{11}+C_{12}) - 2C_{12}^2\right], \tag{3}$$

with

$$\nu_{[110]} = \frac{4C_{12}C_{44}}{C_{11}(C_{11}+C_{12}+2C_{44}) - 2C_{12}^2}. \tag{4}$$

Here, the C_{ij} (in Voigt notation) are the single-crystal elastic constants for the cubic crystal.

B. Ideal shear strength

For the ISS investigation, we performed an affine shear deformation on the close-packed (111) plane along the $[11\bar{2}]$ direction, typically the weakest slip system, i.e., all the atomic planes were involved in the shear deformation. Figure 2 shows the employed monoclinic computational cell in the undistorted state [Fig. 2(a)] and the distorted state [Fig. 2(b)]. In the undistorted state, the three lattice parameters of the monoclinic cell are $(a^0_{\rm mc}, b^0_{\rm mc}, c^0_{\rm mc}) = (\sqrt{2}/2,\ \sqrt{6}/2,\ \sqrt{3})\ a_{\rm fcc}$. It should be noted that the monoclinic cell in the zero-strain state coincides with the orthorhombic representation of the fcc cell (the monoclinic/orthorhombic cell contains six atoms). The lattice vectors $\vec{a}$ and $\vec{b}$ spanning the basal plane are parallel to the $[1\bar{1}0]$ and $[11\bar{2}]$ directions of the fcc structure, respectively, and the lattice vector $\vec{c}$ is perpendicular to this basal plane and parallel to the [111] direction of the fcc structure. In this

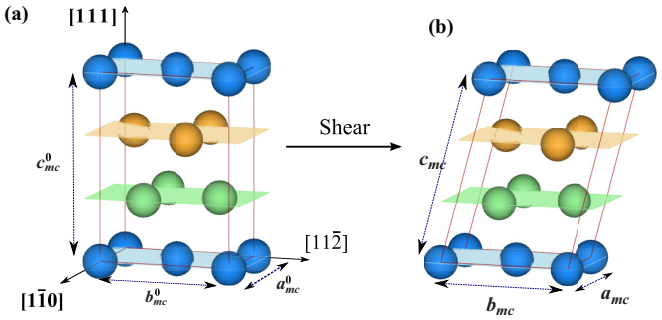

FIG. 2. Monoclinic lattice used for (111)[11$\bar{2}$] pure/simple affine shear. The high-symmetry directions refer to the fcc structure, (a) unstrained, (b) sheared.

work, two modes of shearing were considered following Ogata *et al.* [48]: (i) no relaxation is allowed after shearing, which is defined as *simple affine shear*; (ii) relaxation is allowed after each shear step, the only constraint being the shearing angle, which is identified as *pure affine shear*. The shear stress $\tau(\gamma)$ is given by

$$\tau(\gamma) = \frac{1}{\Omega(\gamma)} \frac{\partial E}{\partial \gamma}, \tag{5}$$

where $\Omega(\gamma)$ is the volume at each shear strain γ. We define the engineering shear strain γ in the same way as Ref. [49]:

$$\gamma = \frac{\text{proj}_{[11\bar{2}]}(\vec{c})}{\text{proj}_{[111]}(\vec{c})}, \tag{6}$$

where $\text{proj}_{[11\bar{2}]}(\vec{c})$ and $\text{proj}_{[111]}(\vec{c})$ denote the projection of the lattice vector $\vec{c}$ onto the [11$\bar{2}$] and [111] directions of the undistorted fcc lattice, respectively. The first maximum on the stress-strain curve (5) determines the ISS τ_{m} with corresponding engineering maximum shear strain γ_{m}.

The shear modulus G relating stress and strain in the linear regime along the [11$\bar{2}$] direction in the (111) plane is given as [49]

$$G_u = \tfrac{1}{3}(C_{11} - C_{12} + C_{44}) \tag{7}$$

and

$$G_r = \frac{3C_{44}(C_{11} - C_{12})}{4C_{44} + C_{11} - C_{12}}. \tag{8}$$

G_u and G_r govern the unrelaxed and relaxed cases, respectively.

C. Half-width of dislocation core

Due to the important role that the dislocation core structure plays in many phenomena of crystal plasticity, considerable interest has been paid to study it [50–52]. Frequently employed theoretical approaches are based on the framework of the Peierls-Nabarro model [53,54]. In these approaches, the half-width of the dislocation core ζ, representing the competition between elastic energy and nonlinear misfit energy (for more details, see Ref. [55]), becomes an important input parameter for the prediction of the Peierls stress [9,55,56]. Following Joós *et al.* [9], the relationship between the half-width of the dislocation core ζ and the ISS τ_m can be described as

$$\zeta = \frac{Kb}{4\pi\tau_m}. \tag{9}$$

Here, K is an energy factor of the dislocation, which depends on the type of dislocation and the crystalline direction of the Burgers vector [56], and b is the magnitude of the Burgers vector. An edge dislocation in the (111) glide plane with dislocation line parallel to the [1$\bar{1}$0] direction and a Shockley partial Burgers vector $\mathbf{b} = \frac{a_{\text{fcc}}}{6}[11\bar{2}]$ was considered in this work. This type of dislocation is very common in fcc crystals [56]. Here, the energy factor K was obtained following Ref. [57].

D. Total-energy calculations

The employed *ab initio* approach is based on DFT [58]. We used the generalized-gradient approximation of the Perdew-Burke-Ernzerhof [59] functional to describe exchange and correlation. The Kohn-Sham equations were solved using the exact muffin-tin orbitals (EMTO) method [60,61]. The scalar-relativistic approximation and the soft-core scheme were used. The problem of chemical disorder in HEAs alloys was treated within the coherent-potential approximation (CPA) and the total energy was computed via the full charge-density technique [62–64]. Since the Curie temperatures of the studied HEAs are well below room temperature [42–44], all calculations were performed in the PM state. The PM state was described by the disordered-local moment model [65] in the CPA framework.

III. RESULTS

A. Lattice constants, elastic moduli, ideal tensile and shear strengths of fcc Ni and Al

Our previous work has shown that the EMTO approach provides an efficient and accurate theoretical tool to study the ITS of bcc crystals [24,66]. To evaluate the accuracy of the present employed method for fcc crystals, we first performed investigations for pure ferromagnetic Ni and nonmagnetic Al. The reason to choose these two elements is the large number of available data from previous investigations.

1. Lattice constants and elastic moduli

The obtained lattice parameter, relaxed tensile modulus for tension along the [110] direction, and the shear modulus relating stress and strain along the [11$\bar{2}$] direction in the (111) plane together with values computed from experimental and theoretical elastic constants are summarized in Table I. For both metals, we can see that our calculated lattice parameters agree very well with the presented experimental and theoretical data. Compared with the experimental results, the deviation is smaller than 1% for Ni, whereas theory and experiment coincide for Al. The predicted tensile modulus $E_{[110]}$, unrelaxed shear modulus G_u, and relaxed shear modulus G_r are in good agreement with those derived from the experiments and theory.

2. Ideal tensile and shear strengths

Turning to the large strain regime, we calculated the ITS for uniaxial loading along the [110] direction and the ISS for the [11$\bar{2}$](111) shear system. In Table II, the calculated (relaxed)

TABLE I. Lattice constant a (in Å), relaxed tensile modulus $E_{[110]}$ (in GPa), and relaxed and unrelaxed shear moduli (in GPa) for Ni and Al from our calculations and available theoretical and experimental data.

System	Method	a	$E_{[110]}$	G_r	G_u
Ni	This work	3.53	256.8	64.3	84.7
	Ref. [67]	3.53	250.8	60.1	79.6
	Ref. [45]	3.52	259.6	...	...
	Expt. Ref. [68]	3.51	250.0	68.7	80.7
Al	This work	4.05	80.9	21.3	25.2
	Ref. [67]	4.04	78.6	25.4	25.4
	Ref. [23]	4.12	...	22.0	27.0
	Ref. [49]	4.05	81.1	29.1	29.2
	Expt. Ref. [69]	4.05	80.1	24.5	24.8

ITS $\sigma_{\rm m}$, unrelaxed (simple affine) ISS $\tau_{\rm m}^u$, relaxed (pure affine) ISS $\tau_{\rm m}^r$, as well as the corresponding ideal strains are listed and compared with previous theoretical data. It can be seen that the $\sigma_{\rm m}$ and $\epsilon_{\rm m}$ for both Ni and Al from our calculations are very close to the reported values from the literature. For Ni, our calculated unrelaxed ISS $\tau_{\rm m}^u$ is somewhat larger than the other theoretical data. However, for the relaxed ISS $\tau_{\rm m}^r$ we note very good agreement. We find that both $\tau_{\rm m}^u$ and $\tau_{\rm m}^r$ of Al are in good agreement with previous calculations. Overall, our calculated ideal shear strains for Ni and Al agree very well with the previously reported data.

The above assessments show that the present method yields a very accurate description of the elastic properties and ideal strengths, which provide the support for the approach used in this paper, and we continue with HEAs.

B. Ideal tensile strength of PM fcc HEAs

Figure 3 displays the tensile stress-strain relationships for fcc CrCoNi, CrFeCoNi, CrMnFeCoNi, and $Cr_{10}Mn_{40}Fe_{40}Co_{10}$ under [110] tension. The corresponding ITSs are tabulated in Table III. The calculated equilibrium lattice constants for these four fcc HEAs are listed in the Appendix. For the ternary alloy CrCoNi, we find that the ITS

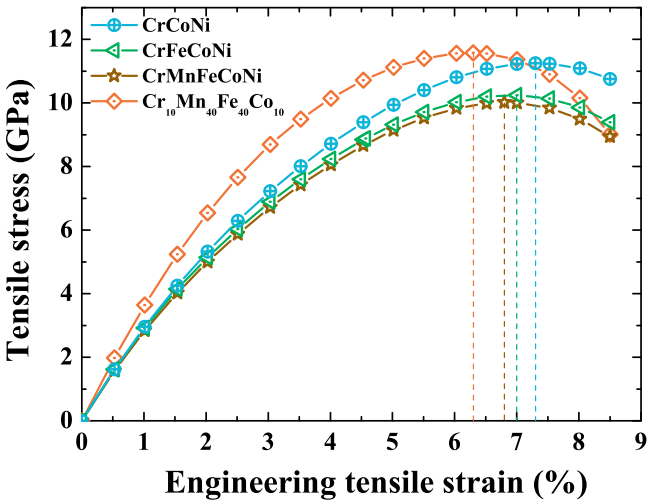

FIG. 3. The tensile stress curves of fcc CrCoNi, CrFeCoNi, CrMnFeCoNi, and $Cr_{10}Mn_{40}Fe_{40}Co_{10}$ under [110] tension as a function of applied strain.

$\sigma_{\rm m}$ is about 11.3 GPa. Compared to CrCoNi, the addition of the fourth element Fe reduces the strength to 10.3 GPa. By adding both Fe and Ni, the strength of CrCoNi decreases to 10.0 GPa. However, if Ni in CrCoNi is substituted with 40 at.% Mn and Fe, we obtain an enhanced ITS amounting to 11.6 GPa for $Cr_{10}Mn_{40}Fe_{40}Co_{10}$. Furthermore, from Fig. 3, we can see that $Cr_{10}Mn_{40}Fe_{40}Co_{10}$ has the smallest ideal tensile strain, whereas CrCoNi has the largest one.

The changes in the lattice parameters of the employed bco computational cell (Fig. 1) as a function of applied tensile strain for $Cr_{10}Mn_{40}Fe_{40}Co_{10}$ under [110] tension are shown in Fig. 4. As is evident, $a_{\rm bco}$ displays a linear increase with increasing strain, whereas $b_{\rm bco}$ and $c_{\rm bco}$ show a nonlinear increase and decrease, respectively. The other three HEAs possess similar lattice parameter changes, and we omit to show them.

Together with the $E_{[110]}$ derived from the computed elastic constants (see the Appendix), we now analyze the dimensionless ITS [73]

$$\sigma^* = \sigma_{\rm m}/E_{[110]}. \tag{10}$$

TABLE II. Ideal tensile and shear strengths (in GPa) as well as the corresponding strains (%) for Ni and Al from our calculations and available theoretical data.

		Tension/[110]		Simple affine shear/ $[11\bar{2}](111)$		Pure affine shear/ $[11\bar{2}](111)$	
System	Method	$\sigma_{\rm m}$	$\epsilon_{\rm m}$	$\tau_{\rm m}^u$	$\gamma_{\rm m}^u$	$\tau_{\rm m}^r$	$\gamma_{\rm m}^r$
Ni	This work	10.1	7.9	7.1	16.2	5.0	15.1
	Ref. [45]	10.5	8.0	...	...	5.1	12.0
	Ref. [46]	9.5	8.0	...	...	...	...
	Ref. [67]	...	...	6.3	16.0	5.1	14.0
	Ref. [70]	...	...	6.3	15.0	5.2	15.0
Al	This work	5.4	14.1	3.8	21.3	3.3	20.2
	Ref. [71]	4.9	14.0	...	...	3.3	18.5
	Ref. [49]	...	...	3.8	21.2	2.8	19.0
	Ref. [67]	...	...	3.8	...	3.0	...
	Ref. [72]	...	...	...	...	3.1	...

TABLE III. Ideal tensile strength σ_m (in GPa), tensile modulus $E_{[110]}$ (in GPa), dimensionless strength σ^*, and resolved shear stress (RSS) for the $[11\bar{2}](111)$ shear system from our calculations (in GPa).

HEAs	σ_m	$E_{[110]}$	σ^*	RSS
CrCoNi	11.3	270.0	0.042	5.3
CrFeCoNi	10.3	275.7	0.037	4.8
CrMnFeCoNi	10.0	262.4	0.038	4.7
$Cr_{10}Mn_{40}Fe_{40}Co_{10}$	11.6	328.1	0.035	5.4

The values are shown in Table III. We find that CrCoNi has the largest σ^* and $Cr_{10}Mn_{40}Fe_{40}Co_{10}$ exhibits the smallest one. We notice that our predicted σ^* for all considered alloys are smaller than the "ideal" value $\sigma^*_{ideal} = 0.05$, which is often used to estimate the ITS of fcc systems [73] on the basis of calculated $E_{[110]}$. For $\sigma^*_{ideal} = 0.05$, the deformation is assumed to follow a sinusoidal stress-strain curve at a constant unit-cell volume [73]. The estimated σ^*_{ideal} differs from our computed value by 20%–40%. This observation indicates that the use of σ^*_{ideal} will lead to a large overestimation of the ITS for HEAs in comparison with the *ab initio* calculations.

C. Ideal shear strength of PM fcc HEAs

The shear stress-strain curves under $[11\bar{2}](111)$ shear deformation are plotted in Fig. 5, and the corresponding ISS values are presented in Table IV. For the pure affine shear mode (relaxed), $Cr_{10}Mn_{40}Fe_{40}Co_{10}$ has the largest maximum strength $\tau^r_m = 5.3$ GPa, and CrMnFeCoNi has the smallest one $\tau^r_m = 4.4$ GPa. Interestingly, we find that the alloying effects

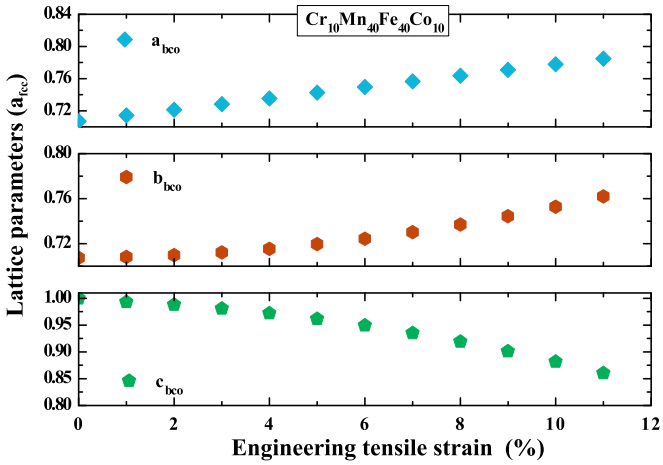

FIG. 4. Variation in the lattice parameters of the bco computational cell (in units of a_{fcc}) for $Cr_{10}Mn_{40}Fe_{40}Co_{10}$ as a function of engineering tensile strain under [110] tension.

on the ISS are the same as on the ITS, i.e., CrFeCoNi and CrMnFeCoNi have smaller ISSs than that of CrCoNi, but the ISS of $Cr_{10}Mn_{40}Fe_{40}Co_{10}$ is the largest. From Fig. 5, we can see that the significantly higher ideal shear strength and strain on the simple affine shear mode are clearly different from those corresponding to the pure affine shear deformation path for each HEA. Compared to τ^r_m, τ^u_m is found to be about two times larger for all considered HEAs. This reflects that the relaxation has a significant effect on the ISS of HEAs.

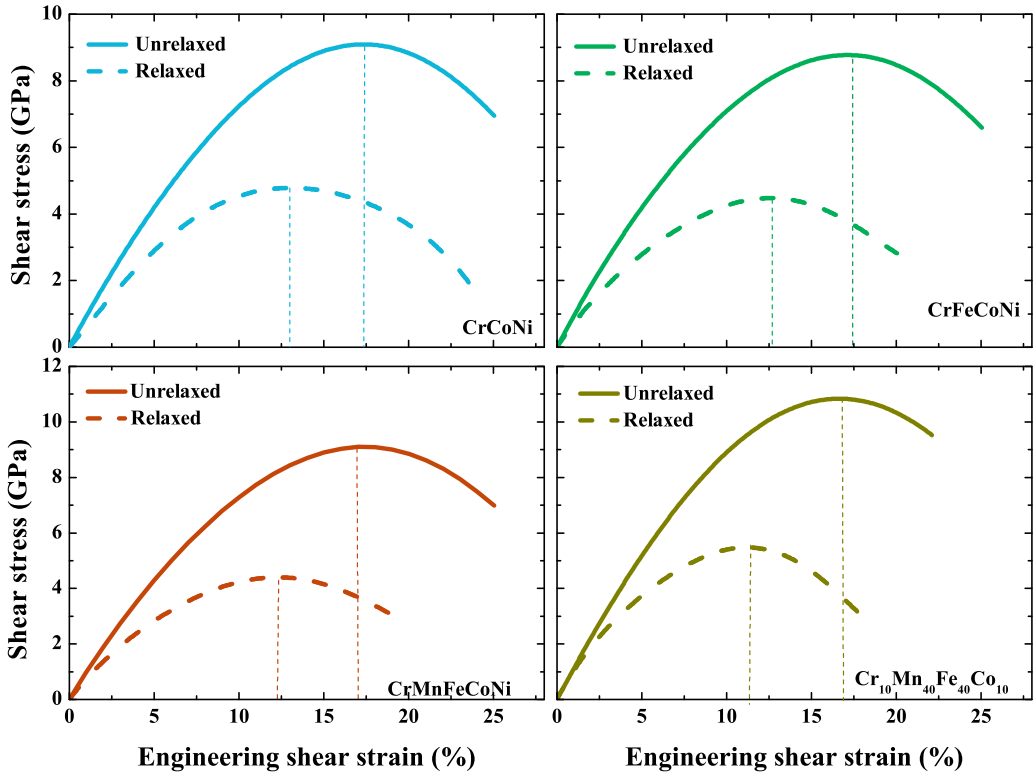

FIG. 5. The shear stress of fcc CrCoNi, CrFeCoNi, CrMnFeCoNi, and $Cr_{10}Mn_{40}Fe_{40}Co_{10}$ under $[11\bar{2}](111)$ shear deformation as a function of applied shear strain.

TABLE IV. Unrelaxed $\tau_{\rm m}^{u}$ and relaxed $\tau_{\rm m}^{r}$ ideal shear strengths (in GPa), unrelaxed G_u and relaxed G_r shear moduli (in GPa) for the $[11\bar{2}](111)$ slip system, unrelaxed τ_u^* and relaxed τ_r^* dimensionless strengths, the ratios $\sigma_{\rm m}/\tau_{\rm m}^{r}$ and B/G, the half-width of the dislocation core (in Å) for an edge dislocation, and the length of the partial Burgers vectors b (in Å). The data in parentheses were derived from the initial slope of the stress-strain curves.

HEAs	$\tau_{\rm m}^{u}$	$\tau_{\rm m}^{r}$	G_u	G_r	τ_u^*	τ_r^*	$\sigma_{\rm m}/\tau_{\rm m}^{r}$	B/G	ζ	ζ_G	b
CrCoNi	9.1	4.8	89.6 (93.0)	61.5 (61.4)	0.104	0.078	2.35	2.20	3.70	2.63	1.44
CrFeCoNi	8.8	4.5	92.6 (95.2)	65.9 (66.5)	0.095	0.068	2.29	1.86	3.90	2.41	1.44
CrMnFeCoNi	9.1	4.4	90.8 (97.4)	61.7 (70.6)	0.100	0.071	2.28	1.68	3.89	2.45	1.44
$Cr_{10}Mn_{40}Fe_{40}Co_{10}$	10.8	5.3	112.0 (112.9)	85.3 (89.6)	0.097	0.062	2.18	1.53	3.70	2.09	1.43

With the above obtained ITSs $\sigma_{\rm m}$ under [110] direction (shown in Table III), we derived the maximum resolved shear stresses on $[11\bar{2}](111)$ via $\sigma_{\rm resol.} = \sigma_{\rm m} \times S$, where S is the Schmid factor of the $[11\bar{2}](111)$ slip system. The calculated data are summarized in Table III. Compared with the obtained ISS $\tau_{\rm m}^{r}$ on $[11\bar{2}](111)$, we find that the resolved shear stress is smaller for each HEA. This suggests that slip intrudes prior to tensile failure for the [110] direction [74]. In other words, all considered HEAs shear in preference to cleaving under [110] tension.

The variation in the lattice parameters of the employed monoclinic computational cell under pure affine shear (Fig. 2) is illustrated in Fig. 6 for $Cr_{10}Mn_{40}Fe_{40}Co_{10}$. One can see that the lattice parameter $a_{\rm mc}$ increases with increasing shear strain, whereas the lattice parameter $b_{\rm mc}$ reduces. Shearing naturally leads to a stretching of the lattice constant $c_{\rm mc}$. We observe that the projection of $\vec{c}$ onto the [111] direction remains virtually unchanged (the filled symbols in Fig. 6). This indicates that the close-packed layer distance is hardly affected by relaxation up to $\gamma^r = 21\%$. It should be noted that the other three HEAs exhibit similar lattice variations, and we omit to show them.

In Table IV, the calculated relaxed and unrelaxed shear moduli G_r and G_u, respectively, obtained from the fcc elastic constants are compared with the values derived from the initial slope of the stress-strain curves. The results from the two approaches are in reasonable agreement with each other. Using the shear moduli obtained from the elastic constants, we calculated the dimensionless ISS [15]

$$\tau_{r/u}^* = \tau_{\rm m}^{r/u}/G_{r/u}, \tag{11}$$

for both relaxed (index r) and unrelaxed (index u) cases. From the data collected in Table IV, we find that the τ_u^* are close to the classic Frenkel estimate $\tau^* \approx 0.11$ [15,75]. For the relaxed state, the obtained τ_r^* are about 0.06–0.07. Our results demonstrate that the estimates of the ISS through the Frenkel model lead to much larger strengths than the *ab initio* calculated ones. For example, if the Frenkel estimate (0.11) were employed, the obtained strength would be up to two times larger than the calculated data.

Using DFT, Ogata *et al.* recently studied the ISS of many crystalline solids exhibiting different crystal structures and bonding types [67], among them simple and transition metals and ceramics. They found that the intrinsic shearability, defined by the maximum shear strain $\gamma_{\rm m}^{r}$ of a crystal, correlates with the degree of directionality of the bonding, i.e., larger shearability corresponds to more directional bonding. Furthermore, they reported a modified Frenkel model, which gives a universal correlation between the ISS and shearability according to

$$\tau_{\rm m}^{r} \approx 2G_r\gamma_{\rm m}^{r}/\pi. \tag{12}$$

The obtained $\tau_{\rm m}^{r}/G_r$ versus $\gamma_{\rm m}^{r}$ from our calculations for the four considered HEAs together with the reported data from Ogata *et al.* are plotted in Fig. 7. Interestingly, in contrast to the classical Frenkel model, our values are nearly on the universal line reported by Ogata *et al.* Moreover, it can be seen that CrCoNi and $Cr_{10}Mn_{40}Fe_{40}Co_{10}$ exhibit the largest and smallest intrinsic shearability, respectively. In other words, CrCoNi may sustain the largest range of shear deformation among these four considered HEAs. The results in Fig. 7 may also indicate that the bonds in CrCoNi are more directional than in $Cr_{10}Mn_{40}Fe_{40}Co_{10}$.

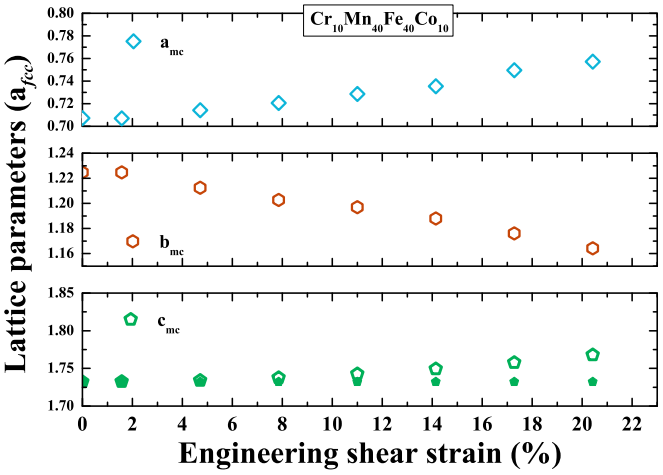

FIG. 6. Variation in the lattice parameters of the monoclinic computational cell (in units of $a_{\rm fcc}$) for $Cr_{10}Mn_{40}Fe_{40}Co_{10}$ as a function of engineering shear strain under $[11\bar{2}](111)$ shear deformation. The solid symbols denote the projection of $\vec{c}$ onto the [111] direction of the undistorted fcc lattice.

D. Half-width of dislocation core

With the help of the obtained ISS $\tau_{\rm m}^{r}$, we derived the half-width of the dislocation core ζ using Eq. (9) for an edge dislocation. The values of ζ for the present four HEAs are listed in Table IV. Our results show that CrFeCoNi and CrMnFeCoNi exhibit similar $\zeta \sim 3.90$ Å, which are about 0.2 Å larger than those of CrCoNi and $Cr_{10}Mn_{40}Fe_{40}Co_{10}$. Furthermore, we find that the values of ζ are approximately 2.6–2.7 times larger than the length of the corresponding Burgers vector b. This indicates that these four HEAs have wide dislocation cores. In

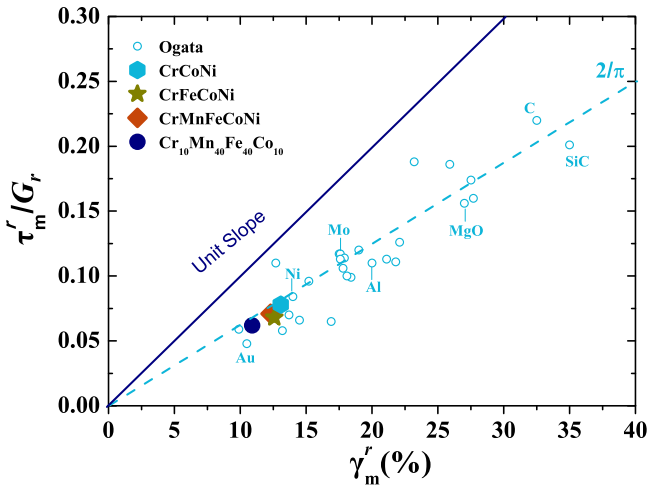

FIG. 7. The obtained τ^r_m/G_r and γ^r_m from our calculations together with the data reported from Ogata *et al.* [67] (open blue circles, selected elements indicated).

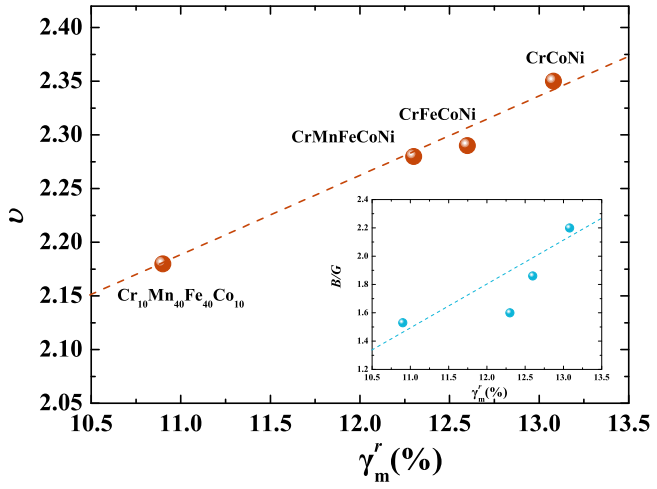

FIG. 8. Correlation between the strength ratio υ and the shear instability γ^r_m. The inset shows the ratio B/G against the shear instability γ^r_m.

Table IV, we also present the estimated ζ_G using $\tau_m \approx 0.11G_r$ on the basis of the classical Frenkel model. Compared to ζ, the estimated ζ_G are smaller. The largest difference in the half-width occurs in $Cr_{10}Mn_{40}Fe_{40}Co_{10}$ and amounts to 44%. The smallest change is in CrCoNi, which is ∼29%. Since the half-width of the dislocation core is involved in many models that are used to obtain critical stresses, our results indicate that large discrepancies regarding the evaluation of the stress may be obtained. For example, if we adopt the analytic formula of Joós *et al.* [9] for wide dislocations, the use of the estimated ζ_G will lead to a larger critical stress compared to that associated with ζ.

E. Intrinsic ductility/brittleness

Ductility is a crucial parameter for the performance of structure materials. Its important role in engineering and materials science has motivated a lot of research intended to develop various types of criteria characterizing the ductility of crystals. For instance, a widely used empirical criterion follows Pugh [76] and involves the ratio of polycrystalline bulk modulus (B) to polycrystalline shear modulus. These moduli are easily obtained from *ab initio* calculations of single-elastic constants through averaging methods [77]. A fracture-related and physically based criterion that involves the ITS and the ISS for assessing intrinsic ductility of a material was introduced by Kelly *et al.* [4]. This criterion attempts to capture the competition between the ease to brittle cleavage fracture (characterized by the ITS) versus the ease to plastic flow (characterized by the ISS) at the tip of a sharp crack.

Using the above obtained ITS and ISS, we calculated the strength ratio

$$\upsilon = \sigma_m/\tau^r_m \tag{13}$$

for the four HEAs, which are presented in Table IV. We observe that the order of υ is CrCoNi > CrFeCoNi > CrMnFeCoNi > $Cr_{10}Mn_{40}Fe_{40}Co_{10}$. A smaller υ is interpreted as an increased probability for crack propagation from the crack tip relative to crack blunting and suggests a reduced ductility. The obtained order indicates that CrCoNi is the most ductile alloy among these four HEAs. In Table IV, we list the values of B/G for comparison. The larger the B/G ratio is, the more ductile is the material [76]. We find that the order of B/G is consistent with the order of υ. In order to confirm the observed trend in the intrinsic ductility, one may envisage transmission electron microscopy experiments of precracked and cross-sectioned specimens to investigate damage and microstructure near and ahead of a sharp crack tip.

Interestingly, we notice that there is a strong linear correlation between strength ratio υ and shear instability γ^r_m, whereas a weak positive correlation is found between B/G and γ^r_m (see Fig. 8). Since γ^r_m measures the bond directionality of materials [67], the observed correlation may indicate that υ not only reveals the ductility, but may also distinguish the directional characteristics of the bonding. The above analysis suggests that υ may be a better indicator of ductility/brittleness for fcc HEAs than previously employed measures. Nevertheless, more studies are needed to further verify this observed correlation.

IV. CONCLUSIONS

Ab initio alloy theory as formulated in the coherent-potential approximation and implemented in the EMTO code was employed to study the ITS and ISS of four random HEAs with fcc structure and PM state. To benchmark the computational accuracy, the ITS and ISS of fcc Ni and Al were calculated. The obtained data for both Ni and Al agree very well with the available theoretical values and thus confirm that our methodology has the accuracy needed for such calculations.

For the HEAs, we found that the ITS of CrCoNi was reduced by adding the fourth element Fe, and was decreased even more when both Fe and Mn were introduced. However, if Ni in CrCoNi was substituted with 40 at.% Mn and Fe to form a nonequimolar HEA $Cr_{10}Mn_{40}Fe_{40}Co_{10}$, the ITS was enhanced. The alloying effects on the ISS are the same as on the ITS. Compared to the unrelaxed ISS, a ∼50% reduction of the ISS was found after relaxation for all considered HEAs. We showed that the derived dimensionless tensile and shear

strengths from our *ab initio* calculations are significantly smaller than the data estimated from two widely used empirical models. We noted that the linear correlation between the dimensionless shear strength and shear instability is consistent with the modified Frenkel model. We observed that CrCoNi has the largest shear instability, whereas $Cr_{10}Mn_{40}Fe_{40}Co_{10}$ has the smallest one. With the help of the computed ISS, we derived the half-width of the dislocation core for an edge dislocation in the (111) plane with dislocation line along the $[1\bar{1}0]$ direction and partial Burgers vector $a_{fcc}/6[11\bar{2}]$. The estimated values from the empirical model were found to be about 29% to 44% smaller than those predicted from our *ab initio* calculations. The alloying effect on the intrinsic ductility was investigated using the strength ratio υ and the empirical criterion B/G. Both criteria suggested that CrCoNi is intrinsically more ductile in comparison with the other three HEAs. Furthermore, we revealed a strong linear correlation between υ and the shear instability, whereas a weak positive correlation was found between B/G and the shear instability. Our observation indicates that υ may be a better measure of ductility compared to B/G for the fcc HEAs.

Our study offers a consistent starting point for further theoretical modeling of the micromechanical properties of the investigated fcc HEAs. In addition, the present results demonstrate that the EMTO-CPA approach provides an efficient and accurate theoretical tool to design both the ITS and the ISS of fcc random solid solutions and uncover the alloying effect on these fundamental physical parameters.

ACKNOWLEDGMENTS

The Swedish Research Council, the Swedish Steel Producers' Association, the Swedish Foundation for Strategic Research, the Swedish Foundation for International Cooperation in Research and Higher Education, and the Hungarian Scientific Research Fund (research Project No. OTKA 109570) are acknowledged for financial support. The simulations were performed on resources provided by the Swedish National Infrastructure for Computing (SNIC) at the National Supercomputer Centre in Linköping.

APPENDIX: LATTICE CONSTANTS AND SECOND-ORDER ELASTIC CONSTANTS OF HEAs

Table V lists the calculated equilibrium lattice constants and elastic constants of the four HEAs using the methodology detailed in Ref. [78].

TABLE V. Computed equilibrium lattice constant (in Å) and second-order elastic constants (in GPa) for HEAs.

HEAs	a_{fcc}	C_{11}	C_{12}	C_{44}
CrCoNi	3.526	290.1	197.3	175.9
CrFeCoNi	3.526	266.6	166.4	177.6
CrMnFeCoNi	3.526	240.0	146.9	179.3
$Cr_{10}Mn_{40}Fe_{40}Co_{10}$	3.505	286.6	154.3	203.6

[1] D. M. Clatterbuck, D. C. Chrzan, and J. W. Morris, Jr., Acta Mater. **51**, 2271 (2003).
[2] N. Nagasako, M. Jahnátek, R. Asahi, and J. Hafner, Phys. Rev. B **81**, 094108 (2010).
[3] A. Kelly and N. H. Macmillan, *Strong Solids* (Clarendon, Oxford, 1986).
[4] A. Kelly, W. R. Tyson, and A. H. Cottrell, Philos. Mag. **15**, 567 (1967).
[5] L. Qi and D. C. Chrzan, Phys. Rev. Lett. **112**, 115503 (2014).
[6] R. Thomson, Physics of Fracture, in *Solid State Physics*, edited by H. Ehrenreich and D. Turnbull (Academic, New York, 1986), Vol. 39, p. 1.
[7] M. J. Jokl, V. Vitek, and C. J. McMahon, Acta Metall. **28**, 1479 (1980).
[8] J. W. Morris, Jr., Z. Guo, C. R. Krenn, and Y. H. Kim, ISIJ Int. **41**, 599 (2001).
[9] B. Joós and M. S. Duesbery, Phys. Rev. Lett. **78**, 266 (1997).
[10] S. Ogata, J. Li, and S. Yip, Phys. Rev. B **71**, 224102 (2005).
[11] W. Xu and J. A. Moriarty, Phys. Rev. B **54**, 6941 (1996).
[12] R. D. Boyer, J. Li, S. Ogata, and S. Yip, Model. Simul. Mater. Sci. Eng. **12**, 1017 (2004).
[13] M. C. Marinica, L. Ventelon, M. R. Gilbert, L. Proville, S. L. Dudarev, J. Marian, G. Bencteux, and F. Willaime, J. Phys.: Condens. Matter **25**, 395502 (2013).
[14] T. Li, J. W. Morris, Jr., N. Nagasako, S. Kuramoto, and D. C. Chrzan, Phys. Rev. Lett. **98**, 105503 (2007).
[15] J. Frenkel, Z. Phys. **37**, 572 (1926).
[16] W. R. Tyson, Philos. Mag. **14**, 925 (1966).
[17] F. Milstein and S. Chantasiriwan, Phys. Rev. B **58**, 6006 (1998).
[18] M. Šob, L. G. Wang, and V. Vitek, Mater. Sci. Eng., A **234–236**, 1075 (1997).
[19] Y. Umeno and T. Kitamura, Mater. Sci. Eng. B **88**, 79 (2002).
[20] K. Yashiro, M. Oho, and Y. Tomita, Comp. Mater. Sci. **29**, 397 (2004).
[21] H. B. Zhou, Y. Zhang, Y. L. Liu, M. Kohyama, P. G. Yin, and G. H. Lu, J. Phys.: Condens. Matter **21**, 175407 (2009).
[22] A. T. Paxton, P. Gumbsch, and M. Methfessel, Philos. Mag. Lett. **63**, 267 (1991).
[23] D. Roundy, C. R. Krenn, M. L. Cohen, and J. W. Morris, Jr., Phys. Rev. Lett. **82**, 2713 (1999).
[24] X. Li, S. Schönecker, J. Zhao, B. Johansson, and L. Vitos, Phys. Rev. B **87**, 214203 (2013).
[25] S. S. Brenner, J. Appl. Phys. **27**, 1484 (1956).
[26] M. B. Lowrya, D. Kienera, M. M. LeBlancb, C. Chisholma, J. N. Florandob, J. W. Morris, Jr., and A. M. Minora, Acta Mater. **58**, 5160 (2010).
[27] C. Lee, X. Wei, J. W. Kysar, and J. Hone, Science **321**, 385 (2008).
[28] J. Y. Kim, D. Jang, and J. R. Greer, Acta Mater. **58**, 2355 (2010).
[29] C. R. Krenn, D. Roundy, M. L. Cohen, D. C. Chrzan, and J. W. Morris, Jr., Phys. Rev. B **65**, 134111 (2002).
[30] J. W. Yeh, S. K. Chen, S. J. Lin, J. Y. Gan, T. S. Chin, T. T. Shun, C. H. Tsau, and S. Y. Chang, Adv. Eng. Mater. **6**, 299 (2004).
[31] B. Gludovatz, A. Hohenwarter, D. Catoor, E. H. Chang, E. P. George, and R. O. Ritchie, Science **345**, 1153 (2014).

[32] Y. Zhang, T. T. Zuo, Z. Tang, M. C. Gao, K. A. Dahmen, P. K. Liaw, and Z. P. Lu, Prog. Mater. Sci. **61**, 1 (2014).

[33] Z. Li, K. G. Pradeep, Y. Deng, D. Raabe, and C. C. Tasan, Nature (London) **534**, 227 (2016).

[34] Y. Deng, C. C. Tasan, K. G. Pradeep, H. Springer, A. Kostka, and D. Raabe, Acta Mater. **94**, 124 (2015).

[35] F. Otto, Y. Yang, H. Bei, and E. P. George, Acta Mater. **61**, 2628 (2013).

[36] A. J. Zaddach, C. Niu, C. C. Koch, and D. L. Irving, JOM **65**, 1780 (2013).

[37] D. Ma, B. Grabowski, F. Körmann, B. Neugebauer, and D. Raabe, Acta. Mater. **100**, 90 (2015).

[38] C. Lu, L. Niu, N. Chen, K. Jin, Y. T. P. Xiu, Y. Zhang, F. Gao, H. Bei, S. Shi, M. R. He *et al.*, Nat. Commun. **7**, 13564 (2016).

[39] C. Niu, A. J. Zaddach, A. A. Oni, X. Sang, J. W. Hurt, J. M. LeBeau, C. C. Koch, and D. L. Irving, Appl. Phys. Lett. **106**, 161906 (2015).

[40] G. Laplanche, A. Kostka, C. Reinhart, J. Hunfeld, G. Eggeler, and E. George, Acta. Mater. **128**, 292 (2017).

[41] B. Gludovatz, A. Hohenwarter, K. V. S. Thirston, H. Bei, Z. Wu, E. P. George, and R. O. Ritchie, Nat. Commun. **7**, 10602 (2016).

[42] M. S. Lucas, L. Mauger, J. A. M. Noz, Y. Xiao, A. O. Sheets, S. L. Semiatin, J. Horwath, and Z. Turgut, J. Appl. Phys. **109**, 07E307 (2011).

[43] M. S. Lucas, D. Belyea, C. Bauer, N. Bryant, E. Michel, Z. Turgut, S. O. Leontsev, J. Horwath, S. L. Semiatin, M. E. McHenry, and C. W. Miller, J. Appl. Phys. **113**, 17A923 (2013).

[44] K. Jin, B. C. Sales, G. M. Stocks, G. D. Samolyuk, M. Daene, W. J. Weber, Y. Zhang, and H. Bei, Sci. Rep. **6**, 20159 (2016).

[45] Y. L. Liu, Y. Zhang, H. B. Zhou, G. H. Lu, and M. Kohyama, J. Phys.: Condens. Matter **20**, 335216 (2008).

[46] M. Černý and J. Pokluda, Phys. Rev. B **82**, 174106 (2010).

[47] V. A. Seeger and O. Buck, Z. Naturforschg. A **15**, 1056 (1960).

[48] S. Ogata, J. Li, and S. Yip, Science **298**, 807 (2002).

[49] M. Jahnátek, J. Hafner, and M. Krajčí, Phys. Rev. B **79**, 224103 (2009).

[50] M. S. Duesbery, Dislocation core and plasticity, in *Dislocations in Solids*, Vol. 8, edited by F. N. R. Nabarro (Elsevier, Amsterdam, 1989), p. 67

[51] V. Vitek, Prog. Mater. Sci. **36**, 1 (1992).

[52] D. Rodney, L. Ventelon, E. Clouet, L. Pizzagalli, and F. Willaime, Acta. Mater. **124**, 633 (2017).

[53] R. Peierls, Proc. Phys. Soc. London **52**, 34 (1940).

[54] F. N. R. Nabarro, Proc. Phys. Soc. London **59**, 256 (1947).

[55] G. Lu, The Peierls-Nabarro model of dislocations: A venerable theory and its current development, in *Handbook of Materials Modeling*, edited by S. Yip (Springer, Dordrecht, 2005), pp. 793–811.

[56] J. P. Hirth and J. Lothe, *Theory of Dislocation* (Wiley, New York, 1992).

[57] Y. T. Chou and G. T. Sha, J. Appl. Phys. **42**, 2625 (1971).

[58] P. Hohenberg and W. Kohn, Phys. Rev. **136**, B864 (1964).

[59] J. P. Perdew, K. Burke, and M. Ernzerhof, Phys. Rev. Lett. **77**, 3865 (1996).

[60] O. K. Andersen, O. Jepsen, and G. Krier, in *Lectures on Methods of Electronic Structure Calculations*, edited by V. Kumar, O. K. Andersen, and A. Mookerjee (World Scientific, Singapore, 1994), p. 63.

[61] L. Vitos, H. L. Skriver, B. Johansson, and J. Kollár, Comput. Mater. Sci. **18**, 24 (2000).

[62] B. L. Gyorffy, Phys. Rev. B **5**, 2382 (1972).

[63] L. Vitos, I. A. Abrikosov, and B. Johansson, Phys. Rev. Lett. **87**, 156401 (2001).

[64] L. Vitos, *Computational Quantum Mechanics for Materials Engineers* (Springer, London, 2007).

[65] B. L. Gyorffy, A. J. Pindor, J. Staunton, G. M. Stocks, and H. Winter, J. Phys. F: Met. Phys. **15**, 1337 (1985).

[66] X. Li, S. Schönecker, J. Zhao, B. Johansson, and L. Vitos, Phys. Rev. B **90**, 024201 (2014).

[67] S. Ogata, J. Li, N. Hirosaki, Y. Shibutani, and S. Yip, Phys. Rev. B **70**, 104104 (2004).

[68] C. Kittel, *Introduction to Solid State Physics* (Wiley, New York, 1986), Vol. 23.

[69] A. G. Every and A. K. McCurdy, *Low Frequency Properties of Dielectric Crystals Second and Higher Order Elastic Constants* (Springer, Berlin, 1992).

[70] S. L. Shang, W. Y. Wang, Y. Wang, Y. Du, J. X. Zhang, A. D. Patel, and Z. K. Liu, J. Phys.: Condes. Matter **24**, 155402 (2012).

[71] D. M. Clatterbuck, C. R. Krenn, M. L. Cohen, and J. W. Morris, Jr., Phys. Rev. Lett. **91**, 135501 (2003).

[72] M. Černý and J. Pokluda, J. Phys.: Condens. Matter **21**, 145406 (2009).

[73] J. W. Morris, Jr., D. M. Clatterbuck, D. C. Chrzan, C. R. Krenn, W. Luo, and M. L. Cohen, Mater. Sci. Forum **426–432**, 4429 (2003).

[74] C. R. Krenn, The Ideal Strength and Mechanical Hardness of Solids, Ph.D. thesis, University of California, 2000.

[75] N. M. Macmillam, J. Mater. Sci. **7**, 239 (1972).

[76] S. F. Pugh, Philos. Mag. **45**, 823 (1954).

[77] R. Hill, Proc. Phys. Soc. Sect. A **65**, 349 (1952).

[78] X. Li, H. Zhang, S. Lu, W. Li, J. Zhao, B. Johansson, and L. Vitos, Phys. Rev. B **86**, 014105 (2012).